HHS Public Access

Author manuscript

Sci Signal. Author manuscript; available in PMC 2022 January 27.

Published in final edited form as:

Sci Signal. ; 14(693): . doi:10.1126/scisignal.abc1940.

Short stature and combined immunodeficiency associated with mutations in RGS10

Ivan K. Chinn[1], **Zhihui Xie**[2], **Eunice C. Chan**[2], **Bianca M. Nagata**[3], **Alexey Koval**[4], **Wei-Sheng Chen**[2], **Fan Zhang**[5], **Sundar Ganesan**[6], **Diana N. Hong**[1], **Motoshi Suzuki**[7], **Glenn Nardone**[7], **Ian N. Moore**[3], **Vladimir L. Katanaev**[4], **Andrea E. Balazs**[1], **Chengyu Liu**[5], **James R. Lupski**[8], **Jordan S. Orange**[9], **Kirk M. Druey**[2,*]

[1]Department of Pediatrics, Texas Children's Hospital and Baylor College of Medicine, Houston, TX 77030, USA.

[2]Lung and Vascular Inflammation Section, Laboratory of Allergic Diseases, NIAID/NIH Bethesda, MD 20892, USA

[3]Infectious Disease Pathogenesis Section, NIAID/NIH, Bethesda, MD 20892, USA

[4]Department of Cell Physiology and Metabolism, Translational Research Centre in Oncohaematology, Faculty of Medicine, University of Geneva, Rue Michel-Servet 1, Geneva CH-1211, Switzerland; School of Biomedicine, Far Eastern Federal University, 8 ul. Sukhanova, Vladivostok 690950, Russia

[5]Transgenic Core, NHLBI/NIH, Bethesda, MD 20892 USA

[6]Biological Imaging Section, NIAID/NIH Bethesda, MD 20892, USA

[7]Protein Chemistry Section, NIAID/NIH, Bethesda, MD 20892, USA

[8]Department of Molecular and Human Genetics and Baylor-Hopkins Center for Mendelian Genomics, Baylor College of Medicine, Houston, TX 77030, USA

[9]Department of Pediatrics, New York Presbyterian Morgan Stanley Children's Hospital and Columbia University College of Physicians and Surgeons, New York, NY 10032, USA

Abstract

We report the clinical and molecular phenotype of three siblings from one family, who presented with short stature and immunodeficiency and carried uncharacterized variants in *RGS10*

*to whom correspondence should be addressed at: 10 Center Drive Room 11N238A, Bethesda, MD 20892. kdruey@niaid.nih.gov; phone 301-435-8875.

Author contributions: Z.X., B.N., E.C.C., A.K., W-S.C., D.N.H., M.S., G.N., F.Z., C.L., K.M.D. performed experiments and analyzed data; S.G., I.C.M., V.L.K. J.R.L., A.E.B., J.S.O. provided reagents, analyzed data, and edited the paper; I.K.C. and K.M.D. supervised the project, performed experiments, analyzed data, and wrote the paper.

Competing interests: J.S.O. has served as a consultant or scientific advisory board member in the area of immunodeficiency for ADMA Biologics Inc., CSL Behring, Enzyvant Inc., GigaGen Inc., Grifols S.A., and The Takeda Pharmaceutical Company Ltd. The other authors declare that they have no competing interests.

Supplementary Materials
figs. S1–10
tables S1–S3
Data Files S1 and S2

(c.489_491del:p.E163del and c.G511T:p.A171S). This gene encodes regulator of G protein signaling 10 (RGS10), a member of a large family of GTPase activating proteins (GAPs) that targets heterotrimeric G proteins to constrain the activity of G-protein-coupled receptors, including receptors for chemoattractants. The affected subjects exhibited systemic abnormalities directly related to the *RGS10* mutations, including recurrent infections, hypergammaglobulinemia, profoundly reduced lymphocyte chemotaxis, abnormal lymph node architecture, and short stature due to growth hormone deficiency. Although the GAP activity of each RGS10 variant was intact, each protein exhibited aberrant patterns of PKA-mediated phosphorylation and increased cytosolic and cell membrane localization and activity compared to the wild-type protein. We propose that the RGS10 p.E163del and p.A171S mutations lead to mislocalization of the RGS10 protein in the cytosol, thereby resulting in attenuated chemokine signaling. This study suggests that RGS10 is critical for both immune competence and normal hormonal metabolism in humans and that rare RGS10 variants may contribute to distinct systemic genetic disorders.

Introduction

The regulator of G protein signaling (RGS) superfamily is a large group of intracellular proteins with diverse functions (1). The 20 canonical RGS proteins are defined by a signature structural motif known as the RGS domain; this motif mediates binding to Gαi/o/z and/or Gαq/11 subunits of heterotrimeric G proteins and GTPase accelerating (GAP) activity (2). The GAP activity of RGS proteins accelerates the conversion of guanosine triphosphate (GTP)-bound Gα subunits to the inactive (GDP-bound) state following G protein-coupled receptor (GPCR) activation. This process typically reduces the duration and amplitude of downstream signaling pathways. The canonical RGS proteins are classified into four sub-groups (RZ, R4, R7, R12) based on structural homology. Additionally, 19 RGS-like proteins that contain an RGS homology (RH) domain have been identified, although not all of them have GAP activity (2). Several of the canonical RGS and RGS-like proteins contain other structural motifs that facilitate the regulation of intracellular processes independent of GAP activity.

Elucidation of the specific signaling pathways controlled by individual RGS proteins has been challenging because most cell types express several RGS proteins with overlapping GAP activities. Nonetheless, considerable progress has been made toward understanding the specificity of many of the RGS proteins and their functions in health and disease. Structural mapping studies suggest that specific amino acid residues within and near the RGS domain determine distinct patterns of G protein selectivity (3–6). Polymorphisms in *RGS* genes are linked to human disease. Bradyopsia, also known as “prolonged electro-retinal response suppression” (PERRS; OMIM#604067), is a rare ophthalmic condition associated with difficulty in detecting moving objects and adjusting to changes in light intensity. This condition was the first monogenic human disease attributed to *RGS* mutations, specifically loss of function mutations in RGS9-1, an R7 family member expressed in the retina (7). Aspects of this human disorder are phenocopied by a genome-wide deletion of *Rgs9-1* in mice (8).

RGS10, RGS12, and RGS14 constitute the R12 subfamily. RGS12 and RGS14 each have a complex structure; RGS12 contains PDZ, phosphotyrosine, Ras-binding, and GoLoco domains that each contribute individually to unique activities (9). For example, the GoLoco domain mediates RGS12 binding to Gα-GDP and inhibits dissociation of GDP from the complex. In mouse striatal neurons, overexpression of RGS12 amplifies β-arrestin-mediated signaling induced by activation of kappa opioid GPCRs (KORs) independently of both its RGS and GoLoco domains. Conversely, *Rgs12*$^{-/-}$ mice exhibit diminished conditioned place aversion, a β-arrestin-dependent behavior, in response to KOR agonists (10).

By contrast, RGS10 lacks additional structural motifs other than the RGS domain and is therefore among the smallest of the known RGS proteins (11). RGS10 is expressed broadly; in mice, functional roles for RGS10 have been reported in bone (12), heart (13), and the immune system (11). RGS10 is widely expressed in leukocytes, including human dendritic cells (14), mouse macrophages (15), and human and mouse lymphocytes (16). Macrophages from *Rgs10*$^{-/-}$ mice exhibit impaired differentiation in response to IL-4 stimulation (15). RGS10 knockdown enhances chemokine-induced chemotaxis and adhesion of human T cell lines in vitro (17). *Rgs10*$^{-/-}$ mice exhibit aberrant T helper type 1 (T_h1) cell trafficking to the brain in the experimental autoimmune encephalitis (EAE) model of the human neuroinflammatory disease multiple sclerosis (18).

Here we describe growth impairment and variable manifestations of immunodeficiency in three male siblings associated with previously undescribed biallelic variants in *RGS10* (OMIM #602056) that segregated with the disease phenotype. We investigated the biochemical activity and cellular functions of the variant RGS10 proteins and their potential contribution to the clinical phenotype of this unique patient cohort.

Results

Clinical and immunological phenotype

Three brothers from Qatar presented for immunologic evaluation due to persistent Epstein-Barr virus (EBV) viremia and lymphadenopathy. The parents denied consanguinity, and two additional older full brothers reported no health issues. At the time of initial assessment, Patient A was five years-old, Patient B was one year-old, and Patient C was nine years-old. All three affected siblings were noted to have diffuse lymphadenopathy and splenomegaly at initial presentation. At follow-up four years later, additional phenotypic features were observed. Patients B and C experienced recurrent pneumonias. Patient B had also developed left ventricular non-compaction cardiomyopathy. None of the three siblings reported cutaneous bacterial, viral, or fungal infections.

Immunologic assessments revealed several abnormalities shared by all three affected brothers (table S1). As a group, they exhibited elevated levels of serum IgG, IgA, and IgM with normal antibody responses to immunization with protein antigens but impaired responses to polysaccharide antigens. Immunofixation electrophoresis confirmed that the IgG was polyclonal. All three subjects were therefore placed on IgG replacement therapy (Fig. 1A). Lymphocyte phenotyping revealed normal B cell counts and B cell subset percentages except for an increased fraction of transitional B cells with normal percentages

of memory B cells. Overall T cell counts were normal albeit with mild $CD4^+$ T cell deficiency and normal $CD8^+$ T cell numbers and percentages, resulting in inverted $CD4^+$-to-$CD8^+$ T cell ratios. Naïve T cell percentages were normal, and T cell proliferative responses to mitogens were within the normal range of the testing laboratory (Fig. 1B). Poor NK cell-mediated cytotoxicity toward K562 target cells was observed (Fig. 1C). Normal Fas-mediated apoptosis was confirmed, thus excluding the diagnosis of autoimmune lymphoproliferative syndrome (ALPS) (table S1) (23). Patient C had an elevated percentage (4.6%) of $CD4^-CD8^-$ TCR$\alpha\beta^+$ T cells, but neither of the other two affected brothers had expanded double-negative T cell percentages (table S1).

Endocrine phenotype

At the time of presentation, all three siblings had been diagnosed with short stature due to growth hormone (GH) deficiency and had been receiving replacement therapy for six months or more (fig. S1). Details regarding length and weight at birth, initial diagnostic evaluation, date of initiation of GH treatment, and growth history prior to GH replacement were not available. To confirm the diagnosis of GH deficiency, we discontinued GH therapy for one month and assessed GH levels in systemic circulation after treatment with clonidine and glucagon. Our results indicated that Patient A (who was evaluated at 4 years, 10 months of age) had mild GH deficiency with a peak post-stimulus serum GH concentration of 6.6 ng/ml (normal >10 ng/ml). The youngest sibling (Patient B) responded normally to stimulation when tested at four years, 11 months of age, with a peak serum GH of 13.6 ng/ml. The oldest brother (Patient C) had severe GH deficiency when tested at 16 years, six months of age, as indicated by a peak post-stimulus serum GH concentration of 1.5 ng/ml. Alternative markers of GH deficiency including serum levels of insulin-like growth factor 1 (IGF-1) and insulin-like growth factor binding protein 3 (IGFBP-3) were detected at the low end of the normal range in all three siblings upon initial presentation; these values remained low throughout the course of GH treatment (table S2).

Genetic analysis

Exome sequencing was performed using blood samples from both parents, the three affected brothers, and two unaffected siblings. We prioritized variants that co-segregated with the phenotype among affected and unaffected family members and in accordance with Mendelian expectations for disease trait patterns of dominant (monoallelic) and recessive (biallelic and hemizygous) inheritance. Additional filtering criteria included minor allelic frequencies (MAFs) in public and internal databases that were less than 0.001 for dominant mode analyses and less than 0.01 for recessive analyses. The dominant mode analyses identified thirteen paternal variants and eight maternal variants shared by all three affected brothers that were not detected in either of the two healthy siblings (table S3). Recessive mode analyses did not uncover homozygous or hemizygous variants that co-segregated with disease among the five siblings. *RGS10* was the only gene identified among the compound heterozygous variants with appropriate segregation. Among the thirteen paternally inherited and eight maternally inherited variants identified by dominant mode analyses, only the PIK3CD p.E525K variant (NM_005026:c.G1573A) was previously identified to be pathogenic (24, 25). The genomes of the father and the three affected sons carried the *PIK3CD* variant, which encodes a constitutively hyperactive p110δ

phosphoinositide 3-kinase (PI3K) protein (OMIM #602839) linked to a unique disorder characterized by recurrent sinopulmonary infections, lymphoproliferative disease, cutaneous herpes virus infections, autoinflammatory disease, and lymphoma known as activated PI3K syndrome, or APDS (#OMIM 615513) (26). Sanger sequencing confirmed the presence of this variant in the father and the three affected siblings but not in the mother or the unaffected siblings (Fig. 1D). At his initial presentation, the father did not have any health issues and lacked any clinical history of chronic or recurrent infections, lymphoproliferative disease, or growth abnormalities although he developed lymphoma later in life at 42 years of age.

Because of the disparate clinical presentations of the father and the three brothers, we focused our attention on the compound heterozygous variants in *RGS10*. Biallelic variants in *RGS10* occur rarely in humans, suggesting that RGS10 function is either necessary for survival, or that there is a lack of redundancy with respect to its critical functions. In the entire genome aggregation database (gnomAD [http://gnomad.broadinstitute.org, version 2.1.1]), only three of the fifteen individual RGS10 protein sequencing-altering variants have been detected in the homozygous state; however, none are frameshift, nonsense, or splicing mutations. The first variant found in our family ("ΔE163"), which was contributed by the mother, results in a deletion of Gln^{163} (NM_001005339:c.489_491del:p.E163del, rs374955363) and has a composite MAF of 0.0002 (0.02 in South Asian populations) in gnomAD. Identification of twelve homozygous carriers of ΔE163 in the database suggests that it does not produce complete loss of RGS10 function. The missense variant (NM_001005339:c.G511T:p.A171S, rs367914663), which is carried by the father, encodes a substitution of Ser in place of Ala^{171} (A171S). This variant is not present in gnomAD. One of the unaffected siblings inherited the gene encoding RGS10(A171S). Each of three affected brothers carried both ΔE163 and A171S as well as the pathogenic variant of *PIK3CD* (Fig. 1E).

Several isoforms of *RGS10* have been described that differ primarily at the N-terminus (11). Isoform 1, also known as *RGS10L* (NM_001005339.1), is a transcript of 910 bp that encodes a 181 amino acid (aa) protein. Isoform 2 (*RGS10S* (NM_002925.3) is a 859 bp transcript that encodes a 167 aa protein (fig. S2A). Consistent with the findings of previous studies of mouse leukocytes (27), we readily detected transcripts encoding isoform 1 in RNA derived from peripheral blood mononuclear cells (PBMCs) from healthy controls and affected patients using isoform-specific PCR primers (fig. S2B). By contrast, isoform 2 was not detected in any of these samples.

Expression of RGS10 in immune cells

To evaluate the impact of the RGS10 variants on the phenotype of these patients, we first analyzed RGS10 expression patterns in leukocytes from healthy controls by flow cytometry (28). RGS10 expression was highest in $CD3^+$ T lymphocytes and comparatively lower in B cells, monocytes, and NK cells; virtually no expression was detected in neutrophils (Fig. 2, A and B and fig. S3). Within the T cell compartment, the highest levels of RGS10 expression were detected in naïve $CD4^+$ and $CD8^+$ ($CD45RA^+$) $CD3^+$ T cells followed by central memory ($CD27^+CD45RA^-$) > effector ($CD27^-CD45RA^+$) > effector memory

($CD27^{-}CD45RA^{-}$) T cell populations (Fig. 2, C and D). RGS10 expression was also detected in follicular helper (T_{fh}) cells ($CD4^{+}CXCR5^{+}$) (fig. S4, A and B), which provide B cell help within lymphoid tissues and are critical for the generation of high affinity antibody responses (29). RGS10 expression in patient-derived PBMC subpopulations was distributed in a manner that was similar to that observed in cells from healthy controls (Fig. 2, E and F). We also evaluated expression of RGS10 in EBV-transformed B cells generated from each affected patient. RGS10 at the appropriate molecular size (~21 kDa) was detected in both patient and control cells at levels that were indistinguishable from one another (Fig. 2, G and H).

Patient-derived lymphocytes display defective chemotaxis

In light of published studies suggesting that RGS10 regulates leukocyte chemotaxis and adhesion (17, 18), we considered the possibility that the RGS10 variants encoded by the genomes of these patients might promote perturbed lymphocyte migration responses to chemoattractants. To test this hypothesis, we first examined chemotaxis of patient-derived EBV-transformed B cells. Compared to the robust chemotaxis of transformed B cells from several different healthy controls as well as those from a patient with the p110δ activating mutation alone, B cells from the patients with biallelic *RGS10* mutations exhibited almost no chemotactic responses to the chemokine CC-motif chemokine ligand 21 (CCL21) (Fig. 3A) or the lipid chemoattractant, platelet activating factor (PAF) (Fig. 3B). Of note, GPCR-mediated chemotaxis signaling has been suggested to proceed through activation of the p110γ PI3K isoform, rather than through activation of p110δ (24, 30, 31). We confirmed this finding in our experiments and showed that CCL21-mediated chemotaxis of B cells from healthy controls was sensitive to a selective inhibitor of p110γ (AS605240) but was not affected by a selective inhibitor of p110δ (idelalisib) (Fig. 3C). The impaired chemotaxis to CCL21 was not due to decreased expression of CCR7, the receptor for CCL21 (Fig. 3D). Together, these results indicate that lymphocyte chemotaxis does not involve p110δ activation and that the diminished responses of B cells with RGS10 mutations are most likely due to a signaling defect located downstream of chemoattractant GPCRs.

Lymphoid tissue abnormalities associated with RGS10 variants

To determine whether the RGS10-associated defects in chemotaxis lead to aberrant lymphocyte trafficking in vivo, we examined lymph node (LN) architecture by immunohistochemistry. When compared to lymphoid tissue from healthy controls, and in contrast to published descriptions of LNs from subjects with APDS (32, 33), LN tissue from Patient B included increased numbers of large follicles with intact B and T cell zones (Fig. 4A) and abundant IgG^{+} plasma cells (Fig. 4B). Within follicles, germinal centers (GCs) were significantly larger in size, with well-demarcated dark zones (DZ, $CD23^{-}$) and light zones (LZ, $CD23^{+}$) (34) and expanded mantle zones (IgD^{+}) compared to LN tissue from healthy controls (Fig. 4, C and D). Overall numbers of GC-associated T_{fh} cells (29) were significantly increased in the follicles of LNs from the patient compared to controls; these cells ($CD4^{+}PD1^{+}$) were concentrated at the periphery of the GC, compared to the more diffuse distribution of these cells in control LN (Fig. 4, E and F). In addition, aggregates of $CD4^{+}PD1^{+}$ cells were observed in extrafollicular areas in patient LN tissue but not in controls. (Fig. 4E). Although no LN tissue was available from Patients A or C, these

findings suggest that trafficking of B and T cells within LNs and GC development are both modulated by RGS10.

RGS10 overexpression inhibits CXLC12-induced expression of growth hormone

Because short stature due to GH deficiency is not a reported feature of APDS (35), we investigated whether RGS10 might contribute to GH deficiency in our patients by regulating GH expression. GH is secreted from somatotrope cells within the anterior pituitary, primarily in response to growth hormone-releasing hormone (GHRH) derived from the hypothalamus (36). GH is also released in response to CXCL12, a chemokine expressed in pituitary tissue whose cognate GPCR, CXCR4, is a potential target of RGS10 (17, 37, 38). We detected immunoreactive RGS10 in tissue sections of normal human anterior pituitary (Fig. 5A). To determine whether RGS10 can regulate chemokine-induced GH expression, we transduced the pituitary adenoma cell line GH4C1 with tat-GFP or tat-RGS10. Stimulation of tat-GFP transduced cells with CXCL12 resulted in a significant and concentration-dependent increase in GH expression (fig. S5, A and B). Consistent with the bimodal or “bell-shaped” outcomes that are characteristic of chemokine-mediated activations (39, 40), we found that intermediate concentrations of CXCL12 promoted maximal GH expression; concentrations that were either higher or lower than 200 nM elicited less pronounced or no increases in GH expression over baseline. Compared to the responses of control cells transduced with tat-GFP, transduction with tat-RGS10 partially blunted GH expression induced by suboptimal concentrations of CXCL12 while significantly reducing GH expression elicited by 200 nM CXCL12 (Fig. 5, B and C). These results indicate that RGS10 overexpression inhibits CXCL12-induced GH expression and suggest that dysregulated RGS10 function in our patients may contribute to the observed clinical GH deficiency.

RGS10 mutations do not affect GAP activity

To determine how the RGS10 sequence variations might contribute to both impaired lymphocyte chemotaxis and GH expression in these patients, we first examined the impact of the specific amino acid substitutions and deletions on RGS10 function in vitro. We expressed hexa-histidine-tagged RGS10 in *E. coli* and purified the recombinant proteins by nickel affinity chromatography. His_6-wild-type (WT), and variant (ΔE163) and (A171S) RGS10 proteins were uniformly soluble and migrated at the anticipated size on SDS chromatography gels (Fig. 6A). To determine whether these mutations affected G protein interactions, we assessed the binding of His_6-RGS10 to Gαi3 using pulldown assays conducted in the presence of GDP alone or GDP with aluminum fluoride and magnesium (AMF), compounds that promote detection of RGS binding to Gα in its transition state conformation between GTP- and GDP-bound states (41). At G protein:RGS10 molar ratios between 0.4 and 0.5, Gαi3 binding to RGS10 decreased by nearly 30% (fig. S6). These results suggested that in this range of molar ratios there is a substantial amount of free RGS10 at equilibrium that is not fully engaged in a complex with Gαi3. Binding assays conducted under these non-saturating conditions (Gαi3: RGS10 molar ratio of 0.4) revealed that each of the variants bound to Gαi3 to an extent that was comparable to the WT protein (Fig. 6, A and B). As expected, neither the WT nor the mutant proteins bound Gαi3 in the presence of GDP alone. A G protein-binding deficient mutant of RGS10 previously

reported to lack GAP activity (E66K) (42) did not bind Gαi3 under any experimental conditions. These results suggest that neither of the patient-associated mutations detected in RGS10 (ΔE163 or A171S) affected the GAP activity of RGS10. To confirm this hypothesis directly, we determined whether the WT or mutant proteins had the capacity to accelerate the GTPase activity of purified recombinant G proteins in experiments that quantitatively evaluated the kinetics of hydrolysis of fluorescently-labeled GTP by Gα. Under saturating (RGS10:G protein molar ratio of 10:1) or non-saturating (1:1 molar ratio) conditions, both of the variants displayed GAP activity (k_{GAP}) that was comparable to that of the WT protein toward all G protein substrates tested, including Gαi1-3 and Gαo1 (Fig. 6, C and D, fig. S7, A–F). Finally, we assessed intracellular G-protein-dependent functions of the RGS10 mutants by evaluating chemokine-induced Erk phosphorylation, a response typically inhibited by RGS protein overexpression (43, 44). Stimulation of HEK293 cells with CXCL12 led to transient increases in Erk phosphorylation that peaked at five minutes and declined thereafter (Fig. 6, E and F). Overexpression of WT or RGS10 mutants inhibited CXCL12-induced Erk phosphorylation to a significant and equivalent extent. Collectively, our findings suggest that diminished chemotaxis of patient-derived lymphocytes is not a result of impaired G protein binding and GAP activity of the ΔE163 and A171S variants of RGS10.

Aberrant phosphorylation of RGS10 mutants

RGS10 is unique among the RGS family members in that it contains a consensus protein kinase A (PKA) phosphorylation sequence (p.KRAS, amino acid residues 173 to 176) near the carboxy-terminus. Burgon *et al.* (45) demonstrated that RGS10 localizes primarily in the cytosol under homeostatic conditions and accumulates in the nucleus when phosphorylated at Ser^{176} by PKA. Although this phosphorylation event does not affect the GAP activity of RGS10 in vitro, it reduces the ability of RGS10 to inhibit GPCR-activated K^+ channel activity in cells, presumably due to nuclear localization. Because the two RGS10 sequence variations identified in our patients lie near the PKA-phosphorylation site, we considered the possibility that these defects might affect PKA-mediated phosphorylation. To explore this hypothesis, we assessed phosphorylation of recombinant RGS10 (WT and mutants) by PKA in vitro; WT RGS10 and RGS10(S176A), the latter variant lacking the known PKA phosphorylation site, were included as positive and negative controls, respectively. We evaluated phosphorylation by immunoblotting using an antibody specific for PKA-phosphorylated substrates that contain a phospho-serine/threonine residue with arginine at the −3 position. As anticipated, WT RGS10 underwent robust PKA-mediated phosphorylation, and no phosphorylation of RGS10(S176A) was detected; these results confirmed the specificity of the assay (Fig. 6G). By contrast, our results demonstrated a 50% reduction in phosphorylation of RGS10(ΔE163) compared to the WT protein (Fig. 6, G and H). Surprisingly, the extent of phosphorylation of RGS10(A171S) was nearly double that of the WT protein. Because the RGS10(A171S) sequence variation includes a new Ser residue, we performed mass spectrometry (LC-MS) to determine whether this introduced a new phosphorylation site. The LC-MS data confirmed that Ser^{176} is the phosphorylated residue in both WT and variant proteins whereas no phosphorylation of Ser^{171} was detected in the A171S variant (fig. S8, A and B). Together, these findings suggest

that the RGS10(ΔE163) and RGS10(A171S) variants may exhibit a more stoichiometrically complex phosphorylation pattern than previously observed in the WT protein.

Anomalous subcellular localization of RGS10 variants

Although several of the characterized RGS proteins are localized at least partially within the cytosol at homeostasis (46–48), they can be recruited to the cell membrane through various mechanisms that facilitate their regulation of GPCR activity (49). For example, although RGS2 has been detected in the cytosol in various cell types (50), nitric oxide (NO) induces its cGMP-dependent protein kinase (PKG)-dependent phosphorylation and localization at the plasma membrane. This response promotes inhibition of vasoconstrictor-induced Gq signaling in vascular smooth muscle cells (51, 52). RGS10 has been detected in both the cytosol (48) and nucleus (47, 53, 54) under homeostatic conditions and can undergo palmitoylation (55), a modification that may promote its affinity for phospholipid membranes (56). The function of RGS10 in the nucleus is largely unknown (46). Because PKA-dependent phosphorylation promotes the nuclear translocation of WT RGS10 (45), we hypothesized that the aberrant phosphorylation of the RGS10 variants might affect their subcellular localization. To test this hypothesis, we expressed myc-RGS10 in COS-7 cells and quantified subcellular localization detected by immunofluorescence staining and confocal microscopy. Under homeostatic conditions, all forms of RGS10 exhibited largely similar localization; either in the cytosol, at the cell membrane, or in the nucleus (Fig. 7, A and B). Treatment with forskolin, a compound that increases PKA activity, resulted in a significant increase in the fraction of WT RGS10 localized in the nucleus. By contrast, significantly more RGS10(ΔE163) or RGS10(A171S) remained in the cytosol of these cells compared to WT RGS10. RGS10(S176A), which does not undergo phosphorylation by PKA at the canonical site, exhibited localization that was similar to WT RGS10 in untreated cells and was not affected by forskolin treatment.

Next, we assessed the subcellular localization of endogenous RGS10 in PBMCs by imaging flow cytometry and confocal microscopy using a rabbit polyclonal antibody specific for the RGS10L isoform. We confirmed the specificity of this antibody using an isotype control antibody (rabbit IgG), which demonstrated no specific staining of PBMCs (fig. S9A). Likewise, we detected RGS10 in lysates of HEK293 cells transfected with myc-RGS10 or naïve B cells by immunoblotting; pre-treatment of the antibody with recombinant His_6-RGS10 before immunoblotting eliminated the signal (fig. S9B). Under homeostatic conditions, RGS10 was localized predominantly in the cytosol and at the membrane in both patient and control PBMCs (Fig. 7C). Treatment of control PBMCs treated with forskolin resulted in a nearly ten-fold increase in the percentage of RGS10 in the nucleus relative to untreated cells (Fig. 7D). By contrast, forskolin had significantly less impact on the nuclear translocation of RGS10 in patient-derived PBMCs; only a two-to-four-fold increase in nuclear localization of RGS10 was observed when compared to cells at baseline (Fig. 7D).

Effect of RGS10 phosphorylation on chemotaxis

Together, our findings indicate that patient-derived lymphocytes may carry an increased pool of cytosolic or cell membrane-associated RGS10 compared to control cells, particularly

when evaluated in the presence of forskolin. Because the GAP activity of the RGS10 variant proteins remained intact, we considered the possibility that these sequence variations lead to diminished chemotaxis based on differential localization. Specifically, we hypothesized that increased quantities of the RGS10(ΔE163) and RGS10(A171S) variant forms of RGS10 would be available at the cell membrane to modulate GPCR activity. To evaluate this possibility, we examined the chemotaxis of T lymphocytes expanded from PBMCs in the presence and absence of forskolin. We found that lymphocytes from two of the three affected patients migrated poorly to CXCL12 compared to those from controls (Fig. 8A). CXCL12-mediated chemotaxis of forskolin-activated T cells from all three patients was significantly diminished compared to the responses of forskolin-activated healthy control cells. Because forskolin promotes nuclear translocation of WT RGS10 but does so less efficiently for RGS10(ΔE163) and RGS10(A171S), we hypothesized that overexpression of the variant proteins in T cells from healthy controls would recapitulate the diminished chemotactic responses observed in patient-derived cells. To test this hypothesis, we transduced control T cells with various tat fusion proteins (Fig. 8B). T cells expressing tat-RGS10 WT exhibited significantly reduced chemotactic responses to CXCL12 compared to cells transduced with a control protein (tat-GFP), whereas cells transduced with the GAP-inactive mutant (E66K) had responses that were similar to those of controls (Fig. 8C). These results suggest that RGS10 inhibits chemotaxis through its GAP activity, a finding that is consistent with previous studies of other RGS proteins (57, 58). Forskolin pretreatment eliminated the differences in chemotaxis between control cells and cells expressing WT RGS10. By contrast, T cells transduced with tat-(ΔE163) or tat-RGS10(A171S) variants demonstrated impaired chemotaxis compared to controls both in the presence and absence of forskolin pre-treatment (Fig. 8D).

Finally, although our previous results suggested that p110δ PI3K isoform (encoded by *PIK3CD*) does not contribute to B cell chemotaxis (Figs. 3A and 3C), these findings do not rule out the possibility that the hyper-active p110δ PI3K(E525K) variant detected in the father and the affected siblings has the capacity to inhibit chemotaxis independently of RGS10. To address this issue, we applied CRISPR-Cas9 to patient-derived B cells using various single guide RNAs (sgRNAs) and oligonucleotide donors (ODN) that were each designed to change one of the *RGS10* variants or the *PIK3CD* variant to that of its respective WT sequence. Detection of a fluorophore-tagged tracrRNA confirmed a high degree (>90%) of cell transfection (fig. S10); none of the three sgRNA/ODN combinations affected the expression of RGS10 (Fig. 8, E and F) or p110δ (Fig. 8, G and H). As anticipated, deep sequencing of genomic DNA extracted from each of the three cell populations transfected with targeted sgRNAs detected increased frequencies of the respective WT (reference) alleles compared to uncorrected patient cells (Fig. 8I–K). Cells in which either the RGS10(ΔE163) or RGS10(A171S) mutation was corrected to the WT *RGS10* allele exhibited significantly higher levels of chemotaxis in response to CCL21 than were observed in uncorrected controls (Fig. 8L). By contrast, cells in which p110δ PI3K(E525K) was corrected to the WT *PIK3CD* allele exhibited chemotaxis to CCL21 that was not significantly different from that observed in their respective uncorrected controls. Together, these results support our hypothesis that the RGS10 variants, but not the p110δ PI3K variant, are critically responsible for the chemotaxis defects observed in patient cells.

Discussion

Here we characterize a clinical phenotype consisting of short stature and immunodeficiency, exhibited by three siblings within a single family. Our study revealed that this phenotype was associated with two previously undescribed or rare variants in RGS10 (ΔE163 and A171S). Analysis of these variants provided evidence for critical functions for human RGS10, including the promotion of adaptive immune responses (T and B cell functions) through control of lymphocyte chemotaxis and support of normal metabolism through regulation of GH expression.

Overall, our mechanistic studies have revealed that: (i) compared to RGS10 WT, larger cytosolic pools of the RGS10(ΔE163) and RGS10(A171S) variants were detected in forskolin-treated cells; (ii) the mislocalization of these variants was associated with severe migration defects in patient-derived lymphocytes. Because all of the patients carry the two mutant alleles, their cells may contain a mix of the two distinct RGS10 variants, but no RGS10 proteins with both mutations. The RGS10(ΔE163) variant was partially resistant to phosphorylation by PKA, which may explain its impaired nuclear translocation in response to forskolin. By contrast, although RGS10(A171S) remained susceptible to PKA-mediated phosphorylation, this variant was also detected primarily in the cytosol in both untreated and forskolin-treated cells. We hypothesize that competing and/or overriding mechanisms that are largely independent of PKA-mediated phosphorylation may determine the localization of the RGS10(A171S) variant. For example, protein localization may be dependent on protein kinase C alpha (PKCα) activation, an event that promotes nuclear export of RGS10 (54). Regardless of the underlying mechanism, our results suggest that accumulation of RGS10(ΔE163) and RGS10(A171S) in the cytoplasm leads to the overabundance of functional RGS10 and thus a higher than normal capacity to exert negative control over chemoattractant-induced GPCR signaling.

Our findings complement earlier studies focused on anomalous subcellular localization of RGS proteins and their contribution to disease pathogenesis. Among these, impaired angiotensin II (Ang II)–induced trafficking of cytosolic RGS5 to the AT_1 receptor at the plasma membrane is observed in vascular smooth muscle cells of spontaneously hypertensive Wistar–Kyoto (WKY) rats (59); these results suggest a role for RGS5 in the dysregulated vasoconstrictor signaling responses characteristic of hypertension. Likewise, two naturally occurring variants of human RGS14 (L505R and R507Q) are less effective at modulating long-term potentiation of hippocampal neurons due to an irreversible accumulation of these variants in the nucleus (60).

We demonstrated that lymphocytes from the clinically-affected siblings exhibited impaired chemotaxis and aberrant localization in lymphoid tissue. The defects in LN architecture may contribute to the systemic immunodeficiency in these patients, which includes impaired responses to vaccination despite polyclonal hypergammaglobulinemia. GC-associated T_{fh} cells, which abundantly express RGS10, were mislocalized in patient LN tissue. GCs harbor the primary site of B cell-T_{fh} interactions that induce differentiation of naïve B cells into antibody-secreting plasma cells (61). Gαi-coupled chemoattractant GPCRs including CCR7, CXCR4, CXCR5, sphingosine 1-phosphate receptor (S1PR1), and EBI2, promote

GC development and maintenance and are thus strong candidates for RGS10-mediated immunoregulation (62). Evidence from mouse models also suggests that RGS proteins can shape adaptive immunity through inhibition of chemotaxis. Specifically, increased numbers of small B cell follicles and disorganized GCs have been identified in mice carrying mutant alleles of *Gnai2* (p.G184S), a form of Gαi2 that is resistant to RGS-mediated GAP activity (63).

Our results also reveal the expression of RGS10 in the anterior pituitary and that RGS10 overexpression inhibits GH production induced by CXCL12. These findings suggest that the disease associated RGS10 variants identified in these patients may contribute to GH deficiency. Numerous stimuli that promote GH secretion, including CXCL12, clonidine, glucagon, and thyrotropin releasing hormone (TRH) act on Gαi and/or Gαq-coupled GPCRs that may be targeted by RGS10 (64, 65). Although the eldest brother responded poorly to GH secretagogues, the youngest patient (Patient B) responded normally when evaluated at four years of age; this result suggests that RGS10-associated GH deficiency might be of delayed onset, and specifically may result from age-dependent changes in pituitary RGS10 expression. *Rgs2, Rgs5, Rgs10,* and *Rgs17* transcripts have been detected in mouse pituitary; of these, *Rgs2* expression undergoes differential and dynamic regulation throughout fetal development (66). Although *RGS10* mRNA has been detected in adult human pituitary tissue (GEO876941, GEO83164164 among others), age-dependent expression has not yet been explored (67). All three siblings exhibited poor responses to GH replacement therapy, as indicated by their persistently low levels of serum IGF-1 and IGFBP-3, which are both markers of the biochemical response to GH. Notably, RGS10 is upregulated in some GH-secreting adenomas (GEO11110179); this result suggests that GH may have a positive impact on RGS10 expression. As such, the overabundance of mutant RGS10 proteins that accumulate in response to exogenous GH treatment might lead to inhibition of its endogenous secretion and promote resistance to therapy.

The enzyme p110δ PI3K is a critical effector of both antigen and growth factor receptors that affect leukocyte maturation, proliferation, and survival (35). Patients with APDS who inherit p.E525K and related mutations in p110δ have variable defects in cellular and humoral immunity, including hypogammaglobulinemia, autoimmune disorders, poor vaccine responses, and reduced numbers of naïve $CD4^+$ and $CD8^+$ T cells and memory B cells (68, 69). However, the father of this family carried the PI3K (E525K) variant but was primarily healthy. Likewise, none of the three affected siblings displayed the full spectrum of symptoms associated with APDS. As a group, these patients presented with several unique clinical features that are not part of APDS as it is currently described. Although growth impairment due to developmental delay has been reported in patients diagnosed with APDS, short stature and GH deficiency have not been associated with this disorder. Further, PI3K p110δ has not been implicated in GH production or secretion. We also note that although all three of the patients with RGS10 variants had a history of recurrent infections of the lung and GI tract and chronic systemic viral infections (EBV), none displayed cutaneous herpes virus or bacterial infections, both of which are prominent features of APDS. These patients were able to mount antibody responses to vaccines containing protein (T-cell dependent) antigens, which is not the case in patients diagnosed with APDS. Finally, although autoantibodies were detected in sera, none of the patients manifested any of the

sequelae of autoimmunity such as cytopenias, renal disease, or arthritis, which are prevalent in APDS patients.

When considered in their entirety, our findings suggest that the two rare RGS10 variants, which segregated with the clinical symptoms of short stature and immunodeficiency, provided critical contributions to the clinical presentation. Although RGS10 defects may modify the course of APDS, it is unclear whether they are sufficient to cause disease on their own. Our experimental data support the hypothesis that the defects in patient cell chemotaxis result from mutations in *RGS10* rather than those in *PIK3CD* (Figs. 3, A and C and 8L). Unfortunately, we were unable to determine the relative importance of the RGS10 variants using samples from the siblings or parents because none of them carried both *RGS10* alleles in the absence of the *PIK3CD* variant. As a further confounding factor, the affected brothers were treated shortly after presentation with mammalian target of rapamycin (mTOR) or p110δ-selective inhibitors, precluding additional evaluation of lymphocyte function. As such, the generation of mouse strains that express each of these two RGS10 variants alone and in combination with one another may be necessary for any further examination of their impact on the immune and endocrine systems.

Materials and Methods

Patients

The parents provided written informed consent for themselves and their five children to participate in a Baylor College of Medicine Institutional Review Board (IRB) approved research protocol (H-29697) for these studies within the Baylor-Hopkins Center for Mendelian Genomics (BHCMG). The consent includes permission to have their clinical and genetic information published in medical and scientific journals. All procedures were performed in accordance with the ethical standards of the IRB and 1964 Helsinki declaration and its amendments.

Exome sequencing

Exome sequencing was performed at the Human Genome Sequencing Center (HGSC) at Baylor College of Medicine through the BHCMG initiative as previously described (70). Briefly, using 1 μg of DNA, we constructed an Illumina paired-end pre-capture library according to the manufacturer's protocol (Illumina Multiplexing_SamplePrep_Guide_1005361_D) with modifications as described in the BCM-HGSC Illumina Barcoded Paired-End Capture Library Preparation protocol. Pre-capture libraries were pooled into 4-plex library pools and then hybridized in solution to the HGSC-designed Core capture reagent (52 Mb, NimbleGen) or 6-plex library pools used the custom VCRome 2.1 capture reagent (42 Mb, NimbleGen) according to the manufacturer's protocol (NimbleGen SeqCap EZ Exome Library SR User's Guide) with minor revisions (71). The sequencing run was performed in paired-end mode using the Illumina HiSeq 2000 platform, with sequencing-by-synthesis reactions extended for 101 cycles from each end and an additional 7 cycles for the index read. With a sequencing yield of 9.1 Gb, the sample achieved 91% of the targeted exome bases covered to a depth of 20X or greater. Illumina sequence analysis was performed using the HGSC Mercury analysis pipeline

(https://www.hgsc.bcm.edu/software/mercury) (72, 73) which moves data through various analysis tools from the initial sequence generation on the instrument to annotated variant calls (SNPs and intra-read in/dels).

Clinical testing

Quantification of serum immunoglobulin levels and specific antibody titers was performed by Quest Laboratories. Clinical enumeration of lymphocyte subsets, assessment of T cell proliferative responses, and evaluation of NK cell cytotoxicity was performed by the Diagnostic Immunology Laboratory at Texas Children's Hospital (Houston, Texas) using Clinical Laboratory Improvement Amendment (CLIA)-certified procedures. Testing for ALPS was performed by the Cincinnati Children's Hospital Diagnostic Immunology Laboratory.

Reagents and chemicals

Forskolin, platelet activating factor (PAF), GDP, $AlC1_3$, NaF, and AS605240 (PI3Kγ inhibitor) were from Sigma. CCL21 and CXCL12 were from R&D Systems. Idelalisib (PI3Kδ inhibitor) was from SelleckChem.

RNA isolation and PCR

RNA was isolated Direct-zol™ RNA kit (Zymo Research). Total RNA (500 ng) was reverse transcribed into cDNA using SuperScript™ IV VILO™ Master Mix (Thermo Fisher). PCR was performed using Platinum™ Hot Start PCR Master Mix and the following primers: RGS10L (isoform 1: forward 5'GCTCCTTCTTCCTCCTCGGG-3', reverse 5'-GTGGATGTCTGACGGCGG-3'; RGS10S (isoform 2): forward 5'-GCAGTGGATTGTTGGTCTGC, reverse 5'-TCGCTGTCGTGGATGTGTTC-3'.

Flow cytometry and intracellular localization

Single samples of approximately thirty (30) mL EDTA-anti-coagulated whole blood were obtained from de-identified adult normal donors from the National Institutes of Health Clinical Center (Protocol Identifier NCT00001846). Mononuclear cells were isolated from peripheral blood using standard Percoll gradient centrifugation methods. Cells were assessed for viability using Zombie Live/Dead, followed by analysis of surface marker expression using the following antibodies: CD3, CD4, CD8, CD19, CD14, CD56, CD45RA, CD27, CXCR5 (Data File S1). Cells were then permeabilized using 0.1% saponin/PBS/milk and stained with goat RGS10 (#C-20, Santa Cruz). Antibody staining was determined using the LSRII flow cytometer and data analyzed using FlowJo software. For intracellular localization experiments PBMCs were permeabilized (Foxp3/Transcription Factor Fixation/Permeabilization Buffer, eBioscience) and stained with rabbit anti-RGS10 (Sigma SAB2105482, 1:500) or rabbit IgG (Sigma), anti-rabbit IgG secondary antibody (ab175471, Abcam), and 2-[4-(Aminoiminomethyl)phenyl]-1*H*-Indole-6-carboximidamide hydrochloride (DAPI, ThermoFisher). Cells were imaged at 60X using an Amnis ImageStreamX MK-II cytometer (Luminex). Acquired data were analyzed for intracellular localization and quantified using IDEAS software (EMD Millipore).

Immunoblotting and immunofluorescence

Cell lysates were prepared using radioimmunoprecipitation (RIPA) buffer containing protease and phosphatase inhibitor cocktails (Complete and PhosStop, respectively, Roche). After addition of SDS sample buffer and boiling for 5 minutes at 95°C, lysates were resolved on 12% NuPAGE gels (ThermoFisher Scientific) and transferred to nitrocellulose membranes. Blots were probed with the appropriate antibodies detected with near infrared-conjugated secondary antibodies using the Li-Cor Odyssey 3000 imager (Li-Cor Biosciences). For immunofluorescence, adherent COS-7 cells were plated directly onto 4-well Chamberwell slides (Nunc). Cells were fixed using PBS containing 4% paraformaldehyde and permeabilized using PBS containing 0.1% Triton X-100. Slides were incubated with blocking buffer (PBS plus 2% BSA/2-5% goat serum/0.1% Tween 20) for one hour at room temperature followed by overnight staining at 4°C in blocking buffer containing rabbit AF488-conjugated c-myc. Cells were then incubated with DAPI (50 μg/ml) for 5 minutes at RT and mounted with glass coverslips using Prolong anti-Fade medium. Images were acquired at 40x magnification using a Leica SP400 epifluorescence microscope or at 63x magnification with a Leica Sp8 DMI8000 confocal microscope.

Cell lines, plasmids, and transfection

HEK293, COS-7, and GH4C1 cells were obtained from ATCC. HEK293 and COS-7 cells were maintained in DMEM containing 10% fetal bovine serum (FBS), L-glutamine, and antibiotics (ThermoFisher). GH4C1 cells were grown in Ham's F12 medium containing 15% horse serum, 2.5% FBS, L-glutamine and antibiotics (ThermoFisher). EBV-transformed B cells were prepared from PBMCs using a standard protocol (74) and grown in RPMI containing 10% FBS, L-glutamine, 10 mM HEPES pH 7, L-glutamine, and antibiotics. COS-7 cells were transfected with pCMV-myc-RGS10L plasmid (Genecopoeia) using Lipofectamine 2000 (ThermoFisher).

Tat fusion proteins

Recombinant tat-FLAG-RGS10 or GFP was generated as described previously (75). The plasmids encoding tat-His-FLAG-RGS10 were the kind gift of Malu Tansey (Emory School of Medicine). Mutations were introduced into the plasmid using the QuikChange mutagenesis kit (Agilent). We added tat proteins (400 nM final concentration) to cells in culture medium for 1–2 hrs. prior to functional assays.

Protein expression, purification, and phosphorylation

RGS10L (WT and mutants) were subcloned into pET28a (Novagen) containing an N-terminal 6-His tag sequence and a stop codon prior to the C-terminal His sequence. Mutations in RGS10 were generated using the QuikChange Site Directed Mutagenesis kit (Agilent Technologies). RGS10 plasmids were transformed into BL21(DE3)pLysS *E. Coli* (Novagen). Cells were grown to log phase in LB medium containing kanamycin (50 μg/ml), and protein expression was then induced with 0.1 mM IPTG overnight at 30°C. Bacteria were pelleted and lysed by freeze-thaw and resuspension into BugBuster solution containing Benzonase (EMD Biosciences) and protease inhibitor cocktail (Roche). Clarified lysates were incubated with Ni^{2+} beads (Roche), and His-RGS10 was eluted using progressively

increasing concentrations of imidazole. Purified His-RGS10 was dialyzed overnight into storage buffer (50 mM HEPES pH 7.5, 100 mM NaCl, 1 mM $MgCl_2$, 1 mM EDTA, 10% glycerol, 1 mM DTT) and stored in aliquots at −80°C. To detect RGS10 phosphorylation, we incubated His-RGS10 (1 μg) in a buffer containing 50 mM Tris-HCl, 10 mm $MgCl_2$, 0.1 mM EDTA, 2 mM DTT, 0.01% Brij 35, 200 μM ATP, and 100 units recombinant catalytic subunit of PKA (NEB) for one hour at 30°C. Reactions were terminated by the addition of SDS sample buffer and boiling. Phospho-RGS10 was detected by SDS-PAGE and immunoblotting with an anti-phospho-PKA substrate antibody. Quantification of phosphoRGS10 bands was performed using ImageStudio software (Li-Cor), and normalized by intensity of bands detected by goat RGS10.

G protein binding and GAP assays

Recombinant RGS10 proteins were incubated with recombinant purified Gαi3 (200 ng, EMD Biosciences) in HKB buffer (76) containing 10 μM GDP, or GDP plus 30 μM $AlCl_3$, and 10 mM NaF, together with Ni^{2+} beads (20 μl of a 50% slurry) for 1 hour at 4°C. Beads were pelleted by centrifugation and washed four times with HKB. Bound proteins were eluted with SDS sample buffer and boiling, followed by resolution on SDS NuPAGE gels and transfer to nitrocellulose. Blots were probed with Gαi3 and RGS10. GAP assays were carried out essentially as described (76). His_6-Gαo1, His_6-Gαi1, His_6-Gαi2 or His_6-Gαi3 (1μM) was mixed with RGS10L, its mutants or equivalent amounts of control protein (mannose binding protein, MBP) (1 or 10 μM) in HKB buffer plus 5 mM $MgCl_2$. BODIPY-FL-GTP (ThermoFisher) was added to the mixture after 10 min preincubation to a final concentration of 1 μM. The kinetics of in vitro G-protein binding to GTP were measured using the VICTOR3 multiwell reader (PerkinElmer).

Mass spectrometry analysis of phosphorylated proteins

Purified recombinant His_6-RGS10L (3 μg) was incubated with the recombinant catalytic subunit of PKA (NEB, 1500 units) for 45 minutes at 30°C. Top-Down liquid chromatography-mass spectrometry (LC-MS) analysis was carried out using an Orbitrap Fusion Lumos mass spectrometer (Thermo Fisher). The sample (50 ng) was injected to a PepSwift monolithic PS-DVB capillary column (Thermo Fisher) and eluted using an acetonitrile gradient. A mass spectrometry scan (MS1) was performed at the 15,000 resolution setting, and 3 data-dependent MS2 scans with Orbitrap at the 120,000 resolution setting after ETD for 8 ms. The data were analyzed with ProSight on the Proteome Discoverer platform (ThermoFisher) using an RGS10L house-build proteoform database and the *E. coli* July 2016 proteoform database (Proteinaceous). To confirm the phosphorylation site(s) of the RGS10 (A171S) variant, PKA-phosphorylated protein was digested with Asp-N protease (Promega), and the protease-digested sample was then cleaned using an OMIX C18 solid phase extraction tip (Agilent). The peptide sample was separated using a Reprosil-PUR AQ-C18 nano-column (New Objective). The MS method contains a survey MS1 scan and was performed using the Orbitrap at the 120,000 resolution setting every 3 seconds, and data-dependent MS2 scans with Orbitrap at the 30,000 resolution setting. For each selected precursor ion, 3 dissociation methods (HCD, ETD, and EThcD) were performed. The data were analyzed using Proteome Discoverer software using the Sequest HT search engine and the ptmRS modification-site localization algorithm.

CRISPR-Cas9 mutagenesis of B cells

The mutations in patient-derived B cells were corrected using CRISPR/Cas9. sgRNAs were designed to cut near each mutation site using CHOPCHOP (https://chopchop.cbu.uib.no), and single-stranded oligonucleotides were used as donors to introduce the desired nucleotide changes (sequences provided in Data File S2). Specific crisprRNAs (crRNAs) and donor oligonucleotides were synthesized and purchased from Integrated DNA Technologies (IDT). Mature sgRNAs were generated by annealing each crRNA with ATTO-550-labeled tracrRNA (IDT #1075928) immediately prior to the transfection experiments. B cells (4–8 × 10^7 cells) were transfected with annealed fluorescent sgRNAs and Cas9 nuclease (IDT #1081059) using the Lonza 4D-Nucleofector × system (Cell Line 4D-Nucleofector™ × Kit S, #VXC-2032). Cas9 nuclease was mixed with the sgRNA complexes at an equimolar ratio and incubated at room temperature for 20 minutes to allow the formation of ribonucleotide-protein (RNP) complex. Cells containing RNP (4.7 μM final concentration) were electroporated using Lonza's pre-set program for human B cells (EO-117); control cells were transfected with ATTO-550-tracrRNA-Cas9 complexes not coupled to a specific sgRNA. Cells were immediately transferred into 6-well dishes containing 5 ml prewarmed RPMI/10% FBS medium and incubated at 37°C and 5% CO_2 for 24 hours prior to chemotaxis assays.

Chemotaxis

T cells were expanded from PBMCs using the T cell activation/expansion kit (Miltenyi Biotec) and cultured in RPMI containing 10% fetal calf serum, antibiotics, 1 mM glutamine, and recombinant human IL-2 (20 U/ml, R&D Systems) (ThermoFisher). Cells were incubated in Transwell inserts (5 μm, Corning) in 24-well plates containing chemokine (CXCL12 400 ng/ml) for 2 hours at 37°C. The percentage of migrated cells was determined by counting viable (Trypan blue negative) cells in the bottom chamber using the Countess II automated cytometer (ThermoFisher) and dividing by the number of cells in a well without insert. In some experiments, T cells were incubated with tat proteins (400 nM) for 2 hours at 37°C in the presence or absence of forskolin (50 μM) prior to the assay. B cells were incubated in Transwell inserts in wells containing CCL21 at the indicated concentrations for 3 hours at 37°C.

Lymphoid tissue histology and immunostaining

Formalin fixed, paraffin-embedded lymph nodes and tonsils from anonymous healthy donors served as control tissue (Zyagen). All samples were sectioned at 5 μm and stained with hematoxylin-eosin (H&E) for examination by light microscopy. Sections were evaluated by a board-certified veterinary pathologist. All images were taken using an Olympus BX51 microscope fitted with an Olympus DP73 camera. Immunohistochemistry (IHC) using a Leica Bond-RX automated system. The Polymer Refine Detection System (Leica) was used to detect the first marker for both single and double immunohistochemistry and the Polymer Refine Red Detection System (Leica) was used for the second marker in double immunohistochemistry. Tissue sections were heated to 72°C for 30 min in Bond Dewax Solution (Leica) and rehydrated with absolute alcohol washes and Immuno Wash (1x, StatLab). Bond Epitope Retrieval Solution 1 (Leica) was applied to sections and heated to

100°C for 20 min for Heat-Induced Epitope Retrieval (HIER). After exposure to peroxide block (Leica) for 5 min, tissues were incubated with the following antibodies: anti-human IgG (1:1000, Dako) or CD3 (RTU, Leica). Antibodies were diluted in Background Reducing Antibody Diluent (Agilent). Following treatment with these primary antibodies, the tissue sections were rinsed with Immuno Wash, treated with a rabbit anti-mouse IgG when appropriate, then incubated with an anti-rabbit HRP polymer (Leica). Colorization was achieved with 3,3'-Diaminobenzidine (DAB) tetrahydrochloride hydrate for 10 min. In the case of double IHC, the DAB protocol was applied first and was followed by Fast Red detection using anti-human CD20 (1:100, Abcam). Colorization was achieved after a 30 min incubation in anti-rabbit AP polymer (Leica) and Fast Red development for 15 min. Slides were counter-stained by using hematoxylin.

Lymphoid tissue immunofluorescence

The epitope retrieval protocol for immunofluorescence was the same as that for immunohistochemistry. Prior to primary antibody incubation, samples were blocked with normal horse serum (3%, Vector) followed by streptavidin and biotin blocking solutions (Vector) for 15 min each. Tissues were then blocked with Serum-Free Protein Block (Agilent) for 30 min and incubated in a primary antibody cocktail solution for 60 min. The following antibodies were used for immunofluorescence: CD4 (1:500, Abcam), PD1 (1:100, BioLegend), IgD (1:500, SouthernBiotech), and CD23 (1:750, Proteintech). Samples were rinsed with Immuno Wash prior to incubation in a cocktail mixture of horse host secondary antibodies for 30 min. The secondary antibodies include 1:300 Alexa Fluor 488 horse anti-rabbit (1:300, Vector), Alexa Fluor 594 horse anti-mouse (1:300, Vector), and biotinylated horse anti-goat (1:200, Vector). Tissues were then incubated in Alexa Fluor 680 Streptavidin (1:500, Thermo Fisher) for 30 min. Slides were counterstained with DAPI (Thermo Fisher Scientific) at 1 μg/mL in 1x PBS for 2 min.

Statistical analysis

Quantified data are expressed as means ± SEM or means ± SD of amalgamated results of three or more biological replicates (each indicated by individual symbols on graphs) from a minimum of 3 independent experiments. All statistical analyses were performed using the GraphPad Prism software package. Shapiro-Wilk tests were applied to determine normality of data. Unpaired, two-tailed Student's *t* test was used for two-group comparative analyses; non-parametric analyses were used for non-normally distributed data. One-sample *t* test was used to compare the differences between one sample and a normalized control (for example, to 100%). For multiple-group comparisons, analysis of variance (ANOVA) was used, with the post hoc multiple comparisons tests as recommended by the software. $P<0.05$ was considered statistically significant.

Supplementary Material

Refer to Web version on PubMed Central for supplementary material.

Acknowledgments:

We thank Helene F. Rosenberg for critical review of the manuscript, Bruce Swihart for biostatistical assistance, and Mohammad Ehlayel, MD (Dept of Pediatrics, Hamad Medical Corporation, Doha, Qatar) for patient referral.

Funding: Jeffrey Modell Foundation Translational Research Award; NIH-NHGRI UM1 HG006542 (Baylor Hopkins Center for Mendelian Genomics), and NIAID/NIH Intramural Program (Z01-AI-000939). The content of this publication does not necessarily reflect the views or policies of the Department of Health and Human Services, nor does the mention of trade names, commercial products, or organizations imply endorsement by the U.S. Government.

Data and Materials Availability:

The mass spectrometry proteomics data have been deposited to the ProteomeXchange Consortium through the PRIDE partner repository with the dataset identifiers PXD023752 and PXD023753. All other data needed to evaluate the conclusions in the paper are present in the paper or the Supplementary Materials. The plasmids require a Material Transfer Agreement from NIAID, NIH.

References and Notes

1. O'Brien JB, Wilkinson JC, Roman DL, Regulator of G-protein signaling (RGS) proteins as drug targets: Progress and future potentials. J Biol Chem 294, 18571–18585 (2019). [PubMed: 31636120]
2. Squires KE, Montanez-Miranda C, Pandya RR, Torres MP, Hepler JR, Genetic Analysis of Rare Human Variants of Regulators of G Protein Signaling Proteins and Their Role in Human Physiology and Disease. Pharmacol Rev 70, 446–474 (2018). [PubMed: 29871944]
3. Soundararajan M et al. , Structural diversity in the RGS domain and its interaction with heterotrimeric G protein alpha-subunits. Proc Natl Acad Sci U S A 105, 6457–6462 (2008). [PubMed: 18434541]
4. Kimple AJ et al. , Structural determinants of G-protein alpha subunit selectivity by regulator of G-protein signaling 2 (RGS2). J Biol Chem 284, 19402–19411 (2009). [PubMed: 19478087]
5. Masuho I et al. , A Global Map of G Protein Signaling Regulation by RGS Proteins. Cell 183, 503–521 e519 (2020). [PubMed: 33007266]
6. Asli A, Sadiya I, Avital-Shacham M, Kosloff M, "Disruptor" residues in the regulator of G protein signaling (RGS) R12 subfamily attenuate the inactivation of Galpha subunits. Sci Signal 11, (2018).
7. Nishiguchi KM et al. , Defects in RGS9 or its anchor protein R9AP in patients with slow photoreceptor deactivation. Nature 427, 75–78 (2004). [PubMed: 14702087]
8. Chen CK et al. , Slowed recovery of rod photoresponse in mice lacking the GTPase accelerating protein RGS9-1. Nature 403, 557–560 (2000). [PubMed: 10676965]
9. Schroer AB et al. , A role for Regulator of G protein Signaling-12 (RGS12) in the balance between myoblast proliferation and differentiation. PLoS One 14, e0216167 (2019). [PubMed: 31408461]
10. Gross JD et al. , Role of RGS12 in the differential regulation of kappa opioid receptor-dependent signaling and behavior. Neuropsychopharmacology 44, 1728–1741 (2019). [PubMed: 31141817]
11. Lee JK, Tansey MG, Physiology of RGS10 in Neurons and Immune Cells. Prog Mol Biol Transl Sci 133, 153–167 (2015). [PubMed: 26123306]
12. Yang S, Li YP, RGS10-null mutation impairs osteoclast differentiation resulting from the loss of [Ca2+]i oscillation regulation. Genes Dev 21, 1803–1816 (2007). [PubMed: 17626792]
13. Miao R et al. , Regulator of G-Protein Signaling 10 Negatively Regulates Cardiac Remodeling by Blocking Mitogen-Activated Protein Kinase-Extracellular Signal-Regulated Protein Kinase 1/2 Signaling. Hypertension 67, 86–98 (2016). [PubMed: 26573707]
14. Shi GX, Harrison K, Han SB, Moratz C, Kehrl JH, Toll-like receptor signaling alters the expression of regulator of G protein signaling proteins in dendritic cells: implications for G protein-coupled receptor signaling. J Immunol 172, 5175–5184 (2004). [PubMed: 15100254]

15. Lee JK, Chung J, Kannarkat GT, Tansey MG, Critical role of regulator G-protein signaling 10 (RGS10) in modulating macrophage M1/M2 activation. PLoS One 8, e81785 (2013). [PubMed: 24278459]
16. Moratz C, Harrison K, Kehrl JH, Regulation of chemokine-induced lymphocyte migration by RGS proteins. Methods Enzymol 389, 15–32 (2004). [PubMed: 15313557]
17. Garcia-Bernal D et al. , RGS10 restricts upregulation by chemokines of T cell adhesion mediated by alpha4beta1 and alphaLbeta2 integrins. J Immunol 187, 1264–1272 (2011). [PubMed: 21705617]
18. Lee JK et al. , RGS10 deficiency ameliorates the severity of disease in experimental autoimmune encephalomyelitis. J Neuroinflammation 13, 24 (2016). [PubMed: 26831924]
19. Phan HTN, Sjogren B, Neubig RR, Human Missense Mutations in Regulator of G Protein Signaling 2 Affect the Protein Function Through Multiple Mechanisms. Mol Pharmacol 92, 451–458 (2017). [PubMed: 28784619]
20. Schwarz E, A gene-based review of RGS4 as a putative risk gene for psychiatric illness. Am J Med Genet B Neuropsychiatr Genet 177, 267–273 (2018). [PubMed: 28544755]
21. Osei-Owusu P, Blumer KJ, Regulator of G Protein Signaling 2: A Versatile Regulator of Vascular Function. Prog Mol Biol Transl Sci 133, 77–92 (2015). [PubMed: 26123303]
22. Phan HTN, Jackson WF, Shaw VS, Watts SW, Neubig RR, Loss-of-Function Mutations in Human Regulator of G Protein Signaling RGS2 Differentially Regulate Pharmacological Reactivity of Resistance Vasculature. Mol Pharmacol 96, 826–834 (2019). [PubMed: 31645376]
23. Rieux-Laucat F, What's up in the ALPS. Curr Opin Immunol 49, 79–86 (2017). [PubMed: 29073495]
24. Lucas CL, Chandra A, Nejentsev S, Condliffe AM, Okkenhaug K, PI3Kdelta and primary immunodeficiencies. Nat Rev Immunol 16, 702–714 (2016). [PubMed: 27616589]
25. Ruiz-Garcia R et al. , Mutations in PI3K110delta cause impaired natural killer cell function partially rescued by rapamycin treatment. J Allergy Clin Immunol 142, 605–617 e607 (2018). [PubMed: 29330011]
26. Jamee M et al. , Clinical, Immunological, and Genetic Features in Patients with Activated PI3Kdelta Syndrome (APDS): a Systematic Review. Clin Rev Allergy Immunol, (2019).
27. Kehrl JH, The impact of RGS and other G-protein regulatory proteins on Galphai-mediated signaling in immunity. Biochem Pharmacol 114, 40–52 (2016). [PubMed: 27071343]
28. Kannarkat GT et al. , Age-related changes in regulator of G-protein signaling (RGS)-10 expression in peripheral and central immune cells may influence the risk for age-related degeneration. Neurobiol Aging 36, 1982–1993 (2015). [PubMed: 25784210]
29. Crotty S, T Follicular Helper Cell Biology: A Decade of Discovery and Diseases. Immunity 50, 1132–1148 (2019). [PubMed: 31117010]
30. Gambardella L, Vermeren S, Molecular players in neutrophil chemotaxis--focus on PI3K and small GTPases. J Leukoc Biol 94, 603–612 (2013). [PubMed: 23667166]
31. Rynkiewicz NK et al. , Gbetagamma is a direct regulator of endogenous p101/p110gamma and p84/p110gamma PI3Kgamma complexes in mouse neutrophils. Sci Signal 13, (2020).
32. Coulter TI et al. , Clinical spectrum and features of activated phosphoinositide 3-kinase delta syndrome: A large patient cohort study. J Allergy Clin Immunol 139, 597–606 e594 (2017). [PubMed: 27555459]
33. Okano T et al. , Hematopoietic stem cell transplantation for progressive combined immunodeficiency and lymphoproliferation in patients with activated phosphatidylinositol-3-OH kinase delta syndrome type 1. J Allergy Clin Immunol 143, 266–275 (2019). [PubMed: 29778502]
34. Victora GD et al. , Identification of human germinal center light and dark zone cells and their relationship to human B-cell lymphomas. Blood 120, 2240–2248 (2012). [PubMed: 22740445]
35. Nunes-Santos CJ, Uzel G, Rosenzweig SD, PI3K pathway defects leading to immunodeficiency and immune dysregulation. J Allergy Clin Immunol 143, 1676–1687 (2019). [PubMed: 31060715]
36. Ooi GT, Tawadros N, Escalona RM, Pituitary cell lines and their endocrine applications. Mol Cell Endocrinol 228, 1–21 (2004). [PubMed: 15541569]

37. Florio T et al. , Chemokine stromal cell-derived factor 1alpha induces proliferation and growth hormone release in GH4C1 rat pituitary adenoma cell line through multiple intracellular signals. Mol Pharmacol 69, 539–546 (2006). [PubMed: 16258074]
38. Barbieri F et al. , Role of stromal cell-derived factor 1 (SDF1/CXCL12) in regulating anterior pituitary function. J Mol Endocrinol 38, 383–389 (2007). [PubMed: 17339401]
39. Nomiyama H et al. , Human CC chemokine liver-expressed chemokine/CCL16 is a functional ligand for CCR1, CCR2 and CCR5, and constitutively expressed by hepatocytes. Int Immunol 13, 1021–1029 (2001). [PubMed: 11470772]
40. Wendel C et al. , CXCR4/CXCL12 participate in extravasation of metastasizing breast cancer cells within the liver in a rat model. PLoS One 7, e30046 (2012). [PubMed: 22253872]
41. Berman DM, Kozasa T, Gilman AG, The GTPase-activating protein RGS4 stabilizes the transition state for nucleotide hydrolysis. J Biol Chem 271, 27209–27212 (1996). [PubMed: 8910288]
42. Alqinyah M, Almutairi F, Wendimu MY, Hooks SB, RGS10 Regulates the Expression of Cyclooxygenase-2 and Tumor Necrosis Factor Alpha through a G Protein-Independent Mechanism. Mol Pharmacol 94, 1103–1113 (2018). [PubMed: 30049816]
43. Berthebaud M et al. , RGS16 is a negative regulator of SDF-1-CXCR4 signaling in megakaryocytes. Blood 106, 2962–2968 (2005). [PubMed: 15998835]
44. Druey KM, Emerging Roles of Regulators of G Protein Signaling (RGS) Proteins in the Immune System. Adv Immunol 136, 315–351 (2017). [PubMed: 28950950]
45. Burgon PG, Lee WL, Nixon AB, Peralta EG, Casey PJ, Phosphorylation and nuclear translocation of a regulator of G protein signaling (RGS10). J Biol Chem 276, 32828–32834 (2001). [PubMed: 11443111]
46. Huang J, Fisher RA, Nuclear trafficking of regulator of G protein signaling proteins and their roles in the nucleus. Prog Mol Biol Transl Sci 86, 115–156 (2009). [PubMed: 20374715]
47. Chatterjee TK, Fisher RA, Cytoplasmic, nuclear, and golgi localization of RGS proteins. Evidence for N-terminal and RGS domain sequences as intracellular targeting motifs. J Biol Chem 275, 24013–24021 (2000). [PubMed: 10791963]
48. Rivero G et al. , Characterization of regulators of G-protein signaling RGS4 and RGS10 proteins in the postmortem human brain. Neurochem Int 57, 722–729 (2010). [PubMed: 20816714]
49. Dulin NO et al. , RGS3 inhibits G protein-mediated signaling via translocation to the membrane and binding to Galpha11. Mol Cell Biol 19, 714–723 (1999). [PubMed: 9858594]
50. Adebiyi A, RGS2 regulates urotensin II-induced intracellular Ca2+ elevation and contraction in glomerular mesangial cells. J Cell Physiol 229, 502–511 (2014). [PubMed: 24105430]
51. Tang KM et al. , Regulator of G-protein signaling-2 mediates vascular smooth muscle relaxation and blood pressure. Nat Med 9, 1506–1512 (2003). [PubMed: 14608379]
52. Sun X, Kaltenbronn KM, Steinberg TH, Blumer KJ, RGS2 is a mediator of nitric oxide action on blood pressure and vasoconstrictor signaling. Mol Pharmacol 67, 631–639 (2005). [PubMed: 15563583]
53. Waugh JL et al. , Regional, cellular, and subcellular localization of RGS10 in rodent brain. J Comp Neurol 481, 299–313 (2005). [PubMed: 15593368]
54. Rimler A, Jockers R, Lupowitz Z, Sampson SR, Zisapel N, Differential effects of melatonin and its downstream effector PKCalpha on subcellular localization of RGS proteins. J Pineal Res 40, 144–152 (2006). [PubMed: 16441551]
55. Castro-Fernandez C et al. , Regulation of RGS3 and RGS10 palmitoylation by GnRH. Endocrinology 143, 1310–1317 (2002). [PubMed: 11897687]
56. Tu Y, Popov S, Slaughter C, Ross EM, Palmitoylation of a conserved cysteine in the regulator of G protein signaling (RGS) domain modulates the GTPase-activating activity of RGS4 and RGS10. J Biol Chem 274, 38260–38267 (1999). [PubMed: 10608901]
57. Reif K, Cyster JG, RGS molecule expression in murine B lymphocytes and ability to down-regulate chemotaxis to lymphoid chemokines. J Immunol 164, 4720–4729 (2000). [PubMed: 10779778]
58. Bowman EP et al. , Regulation of chemotactic and proadhesive responses to chemoattractant receptors by RGS (regulator of G-protein signaling) family members. J Biol Chem 273, 28040–28048 (1998). [PubMed: 9774420]

59. Hong K, Li M, Nourian Z, Meininger GA, Hill MA, Angiotensin II Type 1 Receptor Mechanoactivation Involves RGS5 (Regulator of G Protein Signaling 5) in Skeletal Muscle Arteries: Impaired Trafficking of RGS5 in Hypertension. Hypertension 70, 1264–1272 (2017). [PubMed: 29061726]
60. Squires KE et al. , Human genetic variants disrupt RGS14 nuclear shuttling and regulation of LTP in hippocampal neurons. J Biol Chem, (2020).
61. Zhang Y, Garcia-Ibanez L, Toellner KM, Regulation of germinal center B-cell differentiation. Immunol Rev 270, 8–19 (2016). [PubMed: 26864101]
62. Lu E, Cyster JG, G-protein coupled receptors and ligands that organize humoral immune responses. Immunol Rev 289, 158–172 (2019). [PubMed: 30977196]
63. Hwang IY et al. , An essential role for RGS protein/Galphai2 interactions in B lymphocyte-directed cell migration and trafficking. J Immunol 194, 2128–2139 (2015). [PubMed: 25617475]
64. Kanasaki H et al. , Differential regulation of pituitary hormone secretion and gene expression by thyrotropin-releasing hormone. A role for mitogen-activated protein kinase signaling cascade in rat pituitary GH3 cells. Biol Reprod 67, 107–113 (2002). [PubMed: 12080005]
65. Rodgers RL, Glucagon and cyclic AMP: time to turn the page? Curr Diabetes Rev 8, 362–381 (2012). [PubMed: 22587514]
66. Kim G et al. , Acute stress responsive RGS proteins in the mouse brain. Mol Cells 30, 161–165 (2010). [PubMed: 20680490]
67. Wilson LD et al. , Developmentally regulated expression of the regulator of G-protein signaling gene 2 (Rgs2) in the embryonic mouse pituitary. Gene Expr Patterns 5, 305–311 (2005). [PubMed: 15661635]
68. Tangye SG et al. , Immune Dysregulation and Disease Pathogenesis due to Activating Mutations in PIK3CD-the Goldilocks' Effect. J Clin Immunol 39, 148–158 (2019). [PubMed: 30911953]
69. Burke JE, Structural Basis for Regulation of Phosphoinositide Kinases and Their Involvement in Human Disease. Mol Cell 71, 653–673 (2018). [PubMed: 30193094]
70. Stray-Pedersen A et al. , Primary immunodeficiency diseases: Genomic approaches delineate heterogeneous Mendelian disorders. J Allergy Clin Immunol 139, 232–245 (2017). [PubMed: 27577878]
71. Bainbridge MN et al. , Targeted enrichment beyond the consensus coding DNA sequence exome reveals exons with higher variant densities. Genome Biol 12, R68 (2011). [PubMed: 21787409]
72. Challis D et al. , An integrative variant analysis suite for whole exome next-generation sequencing data. BMC Bioinformatics 13, 8 (2012). [PubMed: 22239737]
73. Reid JG et al. , Launching genomics into the cloud: deployment of Mercury, a next generation sequence analysis pipeline. BMC Bioinformatics 15, 30 (2014). [PubMed: 24475911]
74. Hui-Yuen J, McAllister S, Koganti S, Hill E, Bhaduri-McIntosh S, Establishment of Epstein-Barr virus growth-transformed lymphoblastoid cell lines. J Vis Exp, (2011).
75. Chan EC et al. , Regulator of G protein signaling 5 restricts neutrophil chemotaxis and trafficking. J Biol Chem 293, 12690–12702 (2018). [PubMed: 29929985]
76. Lin C et al. , Double suppression of the Galpha protein activity by RGS proteins. Mol Cell 53, 663–671 (2014). [PubMed: 24560274]

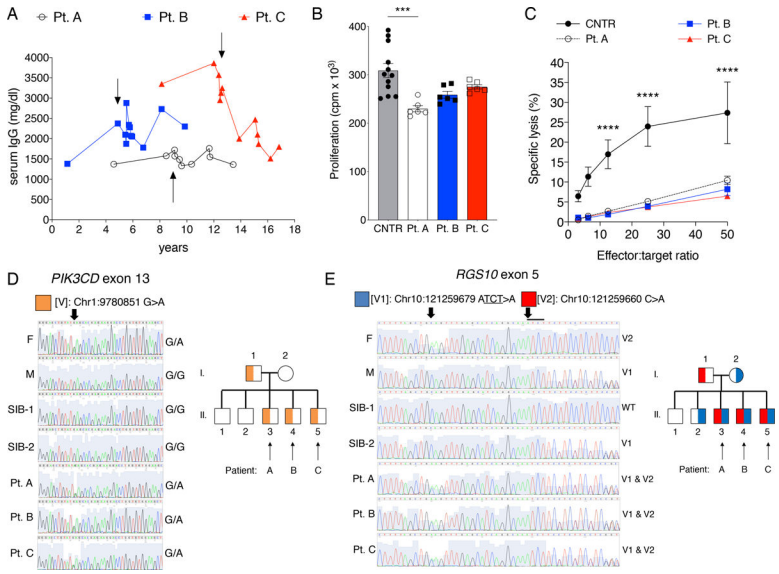

Figure 1. Patient immunophenotyping and genetic data.

(**A**) Serum IgG levels in the affected patients over time. Arrows indicate the age at which each patient began intravenous IgG replacement therapy. (**B**) Proliferation of lymphocytes from each of the 3 siblings and 4 healthy controls assessed by ^{3}H-thymidine incorporation after treatment with phytohemagglutinin (PHA, 10 μg/ml). Mean ± SEM from n=6–12 biological replicates analyzed in n=2 independent experiments. ***P=0.0003 compared to control; Kruskal-Wallis ANOVA, Dunn's multiple comparisons. Non age-adjusted normal range=163507–415087 cpm. (**C**) Cytotoxicity of NK cells isolated from each patient or healthy controls measured by percent lysis of K562 target cells at different effector-to-target (E:T) ratios. Mean ± SEM from n=6–7 biological replicates comparing to 3 healthy controls analyzed in n=3 independent experiments. ****P<0.0001, 2-way ANOVA, Tukey multiple comparisons. (**D-E**) *PIK3CD* and *RGS10* variants revealed by whole exome sequencing and confirmed by Sanger sequencing (chromatograms). Chromosomal coordinates (hg19) of each variant (V) indicated above chromatograms; pedigrees indicate the presence of *PIK3CD* (orange [E525K]) (D) or *RGS10* (blue, V1 [ΔE163], red, V2 [A171S]) (E) variants in each family member (right). Genotypes of patients studied are denoted by arrows. Abbreviations: CNTR, control; cpm, counts per minute; F, father; M, mother; SIB, sibling.

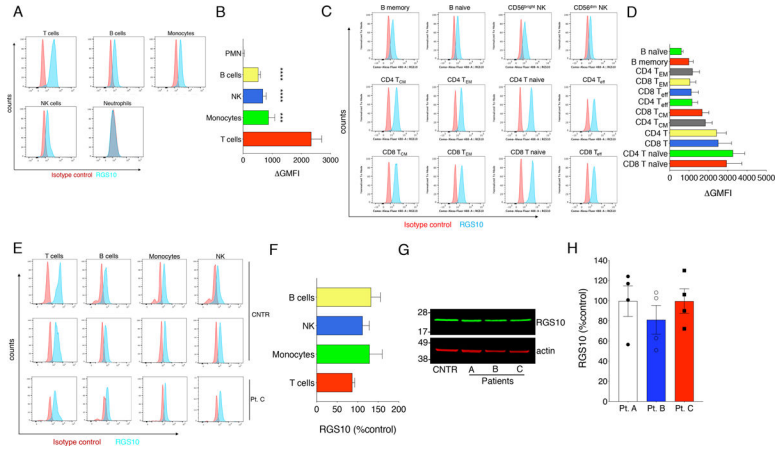

Figure 2. RGS10 expression in immune cells.

(**A-B**) RGS10 expression in leukocyte subsets evaluated by flow cytometry. Representative histograms of geometric mean fluorescence intensity (GMFI) of cells stained with RGS10 (blue) or isotype control IgG (red) (A) and net GMFI (ΔGMFI) quantification (B). Mean ± SEM from n=3–5 healthy control donors. ***P=0.0004, ****P<0.0001 compared to T cells, 1-way ANOVA, Tukey multiple comparisons. (**C-D**) Representative histogram of RGS10 (blue) or isotype control IgG (red) GMFI in T, B, and NK cell subsets (C) and ΔGMFI quantification (D). Mean ± SEM from n=3–4 healthy controls (overall P=0.01, 1-way ANOVA). (**E**) Representative histograms of RGS10 (blue) or isotype control IgG (red) GMFI in peripheral blood mononuclear cells from patient C and 2 different healthy controls (**F**). RGS10 ΔGMFI quantification. Mean ± SEM from n=3 patients and n=5–10 healthy controls; not significant (NS) compared to control, 1-sample t test. (**G-H**) RGS10 expression in control or patient-derived EBV-transformed B cells evaluated by immunoblotting. Representative blot (G) and densitometric quantification (RGS10/actin) (H). Mean ± SEM from n=4 sets of cells; NS vs. control, 1-sample t test.

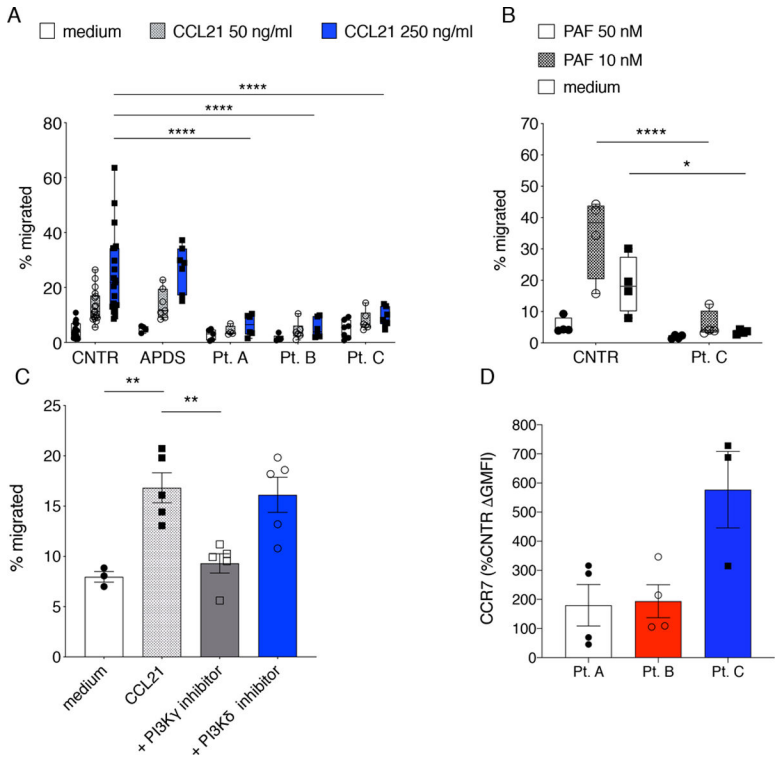

Figure 3. Chemotaxis of patient-derived B cells.

(**A-B**) Chemotaxis of EBV-transformed B cells in response to gradients of CCL21 (A) or platelet activating factor (PAF) (B) in Transwell assays. Mean ± SEM from n=4–14 independent experiments. **P*=0.02, *****P*<0.0001, two-way ANOVA, Tukey (A) or Sidak (B) multiple comparisons. (**C**) CCL21-mediated B cell chemotaxis in cells treated with vehicle alone or pre-treated with AS605240 (PI3Kγ inhibitor, 500 nM) or idelalisib (PI3Kδ inhibitor, 2.5 μM). Mean ± SEM from n=4 independent experiments; ***P*<0.007, 1-way ANOVA, Tukey multiple comparisons. (**D**) CCR7 expression (ΔGMFI) in patient and control B cells determined by flow cytometry. Mean ± SEM from n=3–4 sets of cells. NS compared to control, 1-sample *t* test.

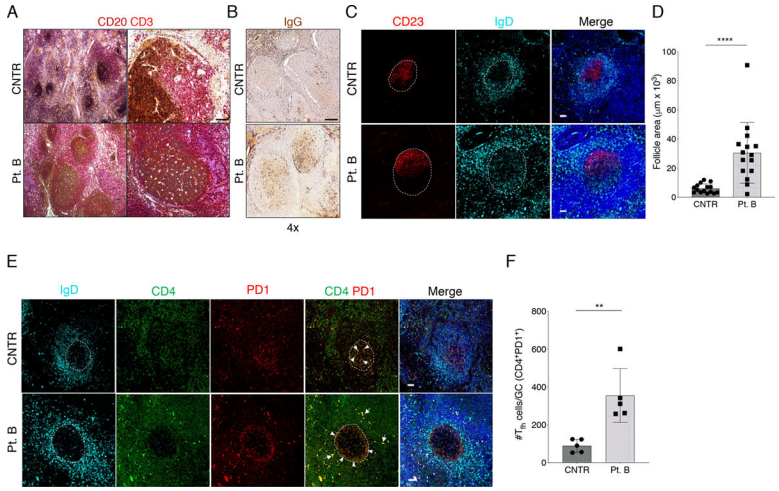

Figure 4. Architecture of lymphoid tissue from a patient with RGS10 variants.

(**A-B**) Immunohistochemical staining of lymph node (LN) tissue from patient B or LN or tonsil from a healthy control stained with CD3 (red) and CD20 (brown) (A) or IgG (brown) (B). Scale bar=200 μm (4x); 50 μm (10x). (**C-D**). Germinal center (GC) organization assessed by immunofluorescent staining of LNs with CD23 (light zone marker, red), IgD (mantle zone marker, light blue) and 4′,6-diamidino-2-phenylindole (DAPI). (**D**) B cell follicle areas (dashed line circles) quantified in LN tissue from patient B and healthy control. Mean ± SD from 15 follicles/section, ****P<0.0001, Mann-Whitney u test). (**E-F**) GC T_{fh} cells identified by CD4 (green), PD1 (red), and IgD (light blue) markers. (E) Double positive cells ($CD4^+PD1^+$) in GCs marked by arrowheads; extrafollicular aggregates by arrows. (F) T_{fh} cells/GC. Mean ± SD from 50–600 cells/follicle in 5 follicles/section. **P=0.008, Mann-Whitney. Scale bar=50 μm, original magnification 63x.

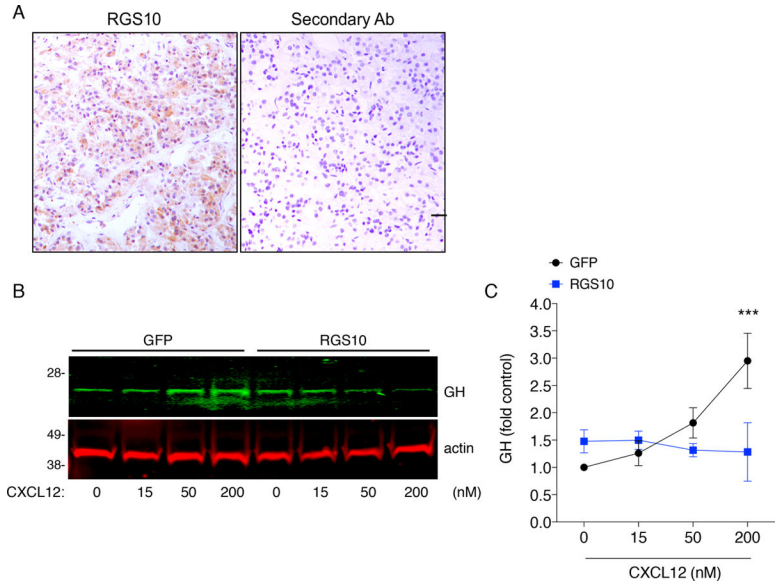

Figure 5. RGS10 overexpression inhibits CXCL12-induced growth hormone (GH) expression.

(**A**) RGS10 expression in normal human anterior pituitary tissue detected by immunohistochemistry (brown). Scale bar=50 μm, original magnification 5x. (**B-C**) GH expression in GH4C1 anterior pituitary cells transduced with tat-GFP or tat-RGS10 and stimulated with CXCL12 at the indicated concentrations. Representative blot (B) and densitometric quantification (GH/actin) (C). Mean ± SEM from n=5–9 independent experiments; ****P*=0.003, 2-way ANOVA, Sidak multiple comparisons.

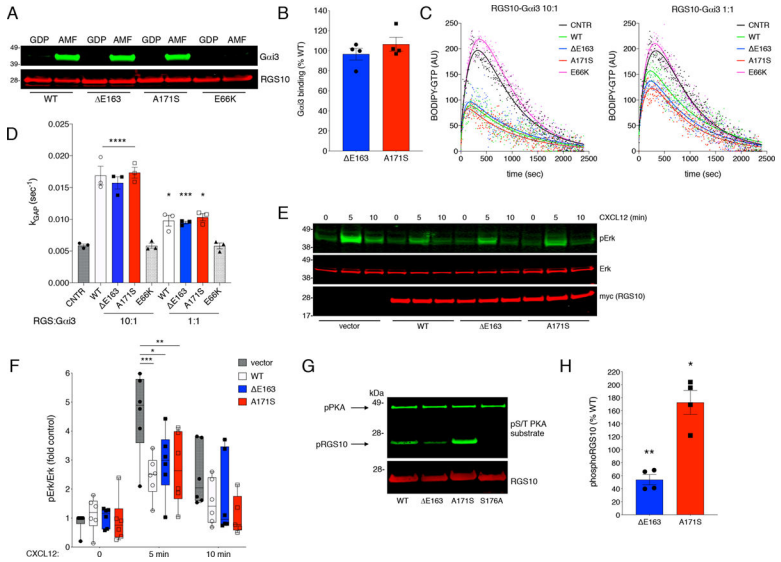

Figure 6. Biochemical activity and phosphorylation of RGS10 variants.

(**A-B**) Binding of His_6-RGS10 to Gαi3 in pulldown assays using nickel-coupled agarose beads. Representative blot (A) and densitometric quantification (B). Mean ± SEM from 4 independent experiments; NS compared to control, 1-sample *t* test. (**C**) Representative binding of BODIPY-GTP (arbitrary units, AU) to Gαi3 (1 μM) over time in the presence or absence of RGS10 (WT or variants, 1 or 10 μM). (**D**) Apparent GTP hydrolysis constants (K_{GAP}). Mean ± SEM from n=3 independent experiments; **P*<0.02; ****P*=0.004, *****P*<0.00001, compared to control, 1-way ANOVA, Dunnett multiple comparisons; NS, WT compared to ΔE163, WT compared to A171S, 1-way ANOVA, Tukey multiple comparisons. (**E-F**) Erk phosphorylation in HEK293 cells transfected with empty vector or myc-RGS10L (WT or variants) and stimulated with CXCL12. Representative blot (E) and quantification by densitometry (pErk/Erk) (F). Mean ± SEM from n=3 independent experiments; **P*=0.01, ***P*=0.005, ****P*=0.001, 2-way ANOVA, Tukey multiple comparisons. (**G-H**) Phosphorylation of RGS10 by PKA in vitro detected by phosphoSer/Thr PKA substrate antibody. Representative blot (G) and densitometric quantification (phosphoRGS10/total RGS10) (H). Mean ± SEM from n=3 independent experiments; **P*=0.03, ***P*=0.009 compared to control, 1 sample *t* test. Arrows denote phosphorylated RGS10 (23 kDa) and autophosphorylated PKA (45 kDa).

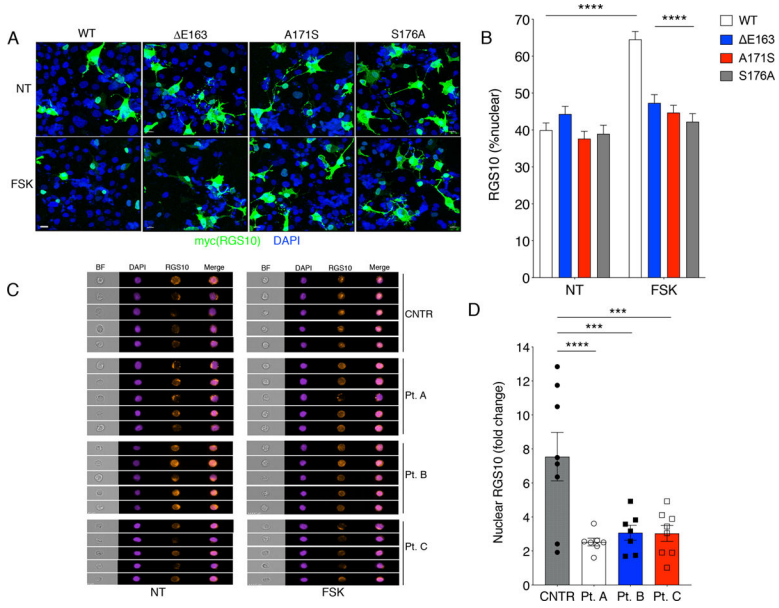

Figure 7. Mislocalization of RGS10 variants.

(**A-B**) Immunofluorescence staining of COS-7 cells transfected with myc-RGS10 (WT or variants) and immunostained with myc (green) and DAPI (blue). (NT, not treated; FSK, forskolin). Representative images (A) and quantification of percentage of nuclear RGS10 (B). Mean ± SEM of 57–83 cells/condition from n=3 independent experiments; **** P<0.00001, 2-way ANOVA, Tukey multiple comparisons. Scale bar=20 μm, original magnification 63x. (**C-D**) Localization of endogenous RGS10 in PBMCs left untreated (NT) or stimulated with forskolin by flow cytometry and confocal microscopy. Representative brightfield (BF) images, RGS10 immunostaining (orange) and DAPI (pink) (C). Fold increase in nuclear RGS10 localization in FSK-treated cells compared to untreated controls (D). Mean ± SEM from n=3 independent experiments. *** P<0.002, **** P=0.0007 compared to control, 1-way ANOVA, Dunnett multiple comparisons.

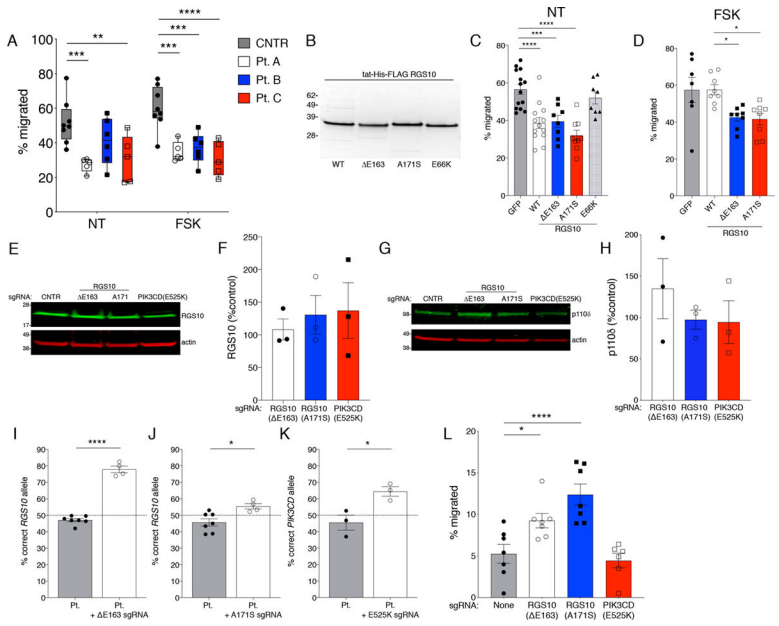

Figure 8. Role of RGS10 phosphorylation in regulating chemotaxis.

(**A**) CXCL12-induced chemotaxis of T cells from each patient or healthy controls (n=3) that were not pre-treated (NT) or pre-treated with forskolin (FSK) prior to the assay. Mean ± SEM from 5–8 independent experiments. ***P*=0.009, ****P*<0.002, *****P*=0.0002 2-way ANOVA, Tukey multiple comparisons. (**B**) Coomassie-stained gel of purified tat-RGS10 WT, ΔE163, A171S, and E66K proteins. (**C**) CXCL12-induced chemotaxis of T cells transduced with tat-GFP or tat-RGS10 (WT or variants) to CXCL12. Mean ± SEM from n=4–12 independent experiments. ****P*=0.002, *****P*<0.0002, 1-way ANOVA, Tukey multiple comparisons. (**D**) CXCL12-induced chemotaxis of tat protein-transduced T cells from healthy controls pretreated with forskolin. Mean ± SEM of n=4–8 independent experiments, **P*<0.04, 1-way ANOVA, Tukey multiple comparisons. (**E-F**) RGS10 expression in patient B cells transfected with the specific sgRNAs indicated. Representative blot (E) and densitometric quantification (RGS10/actin) (F). Mean ± SEM of n=3 independent experiments. NS compared to control, 1-sample *t* test. (**G-H**) p110δ expression in patient B cells transfected with the specific sgRNAs indicated. Representative blot (G) and densitometric quantification (p110δ/actin) (H). Mean ± SEM of n=3 independent experiments. NS compared to control, 1-sample *t* test. (**I-K**) Frequencies of detection of the correct (reference) allele [RGS10(ΔE163 (I), RGS10(A171S) (J) or PIK3CD(E525K) (K)] in patient B cells transfected with the sgRNAs indicated. Mean ± SEM from n=3–6 biological replicates per group. **P*<0.02, *****P*<0.0001 compared to uncorrected patient controls, unpaired t test. (**L**) CCL21-induced chemotaxis of patient B cells transfected with the sgRNAs indicated. Mean ± SEM from n=6 independent experiments. **P*=0.03, *****P*=0.0002 compared to uncorrected patient controls, 1-way ANOVA, Dunnett multiple comparisons.